Calibration and test of the tangential phase contrast imaging diagnostic on CDX-U[a)]

E. Lo, R. Nazikian, D. Stutman, W. Choe, and R. Kaita
Princeton Plasma Physics Laboratory, Princeton University, Princeton, New Jersey 08543-0451

(Received 14 May 1996; accepted for publication 14 June 1996)

A novel CO_2 laser-based tangential imaging diagnostic was completely calibrated and the system was tested on CDX-U plasmas. It was shown that localized, two-dimensional images of the plasma electron density fluctuations in the tokamak core can be obtained from a tangential imaging beam [E. Lo, J. Wright, and R. Nazikian, Rev. Sci. Instrum. **66**, 1180 (1995)]. A variation of the Zernike phase mirror is used. Test measurements made on sound waves verify that the system will image phase variations placed at the object plane. An absolute sensitivity of $\approx 1\times 10^7$ $\mathrm{cm}^{-3}/\sqrt{\mathrm{Hz}}$ was determined. A series of plasma measurements made on CDX-U is described. Results show that the plasma fluctuations are two to three orders of magnitude above the noise floor of the diagnostic. It is also verified that a high-pass cut-off wave number (from ≈ 1 to 8 cm^{-1}) for the fluctuations can be selected by translating the phase mirror. The density fluctuation k spectrum is measured and found to peak at ≈ 1–3 cm^{-1}. © *1997 American Institute of Physics.* [S0034-6748(97)00202-5]

I. INTRODUCTION

A novel CO_2 laser-based tangential phase contrast imaging (PCI) system was developed on the current drive experiment-upgrade (CDX-U) tokamak[1] to measure two-dimensional images of density fluctuations. Unlike other PCI systems,[2–4] the laser beam is passed horizontally through the CDX-U tokamak in an attempt to achieve a localized measurement. It was shown in earlier papers[5,6] that, with the proper phase mirror, recovery of an image of the density fluctuation profile at the tangency plane (the plane where the beam is tangent to the toroidal magnetic field lines) is possible. A successful ''proof-of-principle'' test of the diagnostic on CDX-U is desirable so that it can be used for transport and confinement studies.

Each of the instrumental components of the system was characterized, which then permits calculation of the system responsivity and absolute sensitivity. Methods used for locating the image plane, required for accurate imaging, are discussed. The final method involves a measurement of beam diffraction that demonstrates the close-to-ideal performance of the diagnostic. Extensive tests of imaging using sound waves in air were done in order to prove that imaging of phase objects is indeed occurring. Most important, the high-pass wave number cutoff of the system, required by the localization scheme, is verified. With the components of the diagnostic thoroughly characterized and its capabilities tested, assurance is provided that plasma fluctuations can be imaged.

The plasma measurements described in this article verify two important components of the proof-of-principle. The first is simply that the system sensitivity is sufficient for plasma fluctuations. Despite the additional noise inflicted on the system by tokamak operation, the plasma signal is found to be at least two to three orders of magnitude above the noise floor. A demonstration that the measured signal represents plasma is clearly provided by observation of sawteeth which were correlated with soft x-ray emissions. Cutoff of the plasma signal as the phase mirror was scanned provided the second verification. The plasma density fluctuation k spectrum can be high pass filtered using the phase mirror, with the cut-off wave number set by the phase mirror position. An approximate measurement of the k spectrum was possible, with the significant finding that most of the fluctuation power lies within range of the imaging system, i.e., from 1 to 8 cm^{-1}.

II. DESCRIPTION OF THE EXPERIMENT

A. Optical layout

The optical layout of the system is shown in Fig. 1. Mirrors M1–M5 propagate the first half of the beam a distance of ≈ 8 m, which removes much of the scattered light from the beam and improves the purity of its TEM_{00} mode. A telescopic arrangement of two lenses L1 and L2, with focal lengths of -10 and $+50$ cm, respectively, expands the beam by a factor of 5. This two lens expander is much easier to align, and less sensitive to misalignment than a previously used off-axis parabolic mirror. All optic apertures up to L2 satisfy the $d/w > 4.6$ criterion,[7] and thus are not expected to perturb the mode quality.

Lens L2 significantly reduces the aperture of the expanded beam. The result is a circular beam with an intensity decrease of $\approx 40\%$ from its peak to the edge sightline. Beam profile flatness is desired so that all of the sightlines will have roughly the same dc intensity on the detector elements. Mirrors M6 and M7 steer the expanded beam through the tokamak plasma to the objective lense (L3).

The object plane (labeled ''O'') contains the density fluctuations to be imaged ($\tilde{n}$) and is located midway between the two steering mirrors. It occurs at the point of tangency between the laser beam and the magnetic field lines (i.e., B_0), and is also termed the tangency plane.

To a first approximation, the beam at the objective lens carries a projection of all the apertures and phase variations

[a)]The abstract for this article was published in Rev. Sci. Instrum. **68**, 689 (1997).

 © 1997 American Institute of Physics

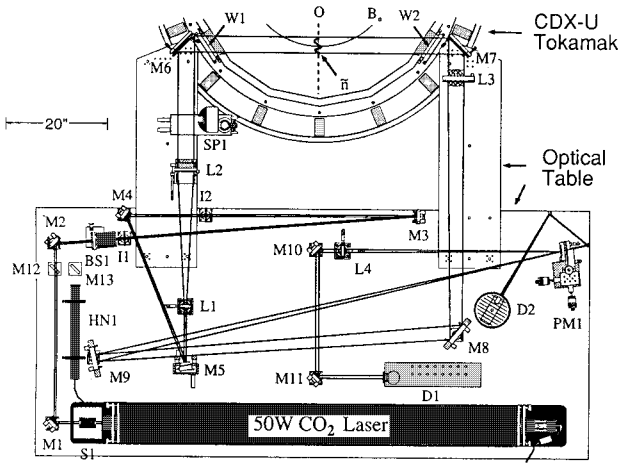

FIG. 1. Optical layout of the system.

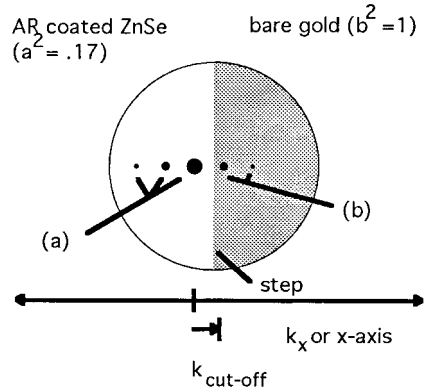

FIG. 2. Schematic diagram of the phase mirror. (a) The laser beam focal spot along with some higher k_x scattered components; (b) the scattered components on the gold side that is also phase shifted by 28°.

between the objective and the expander lens, L2. The limiting aperture is the objective lens that has a 9.3 cm (≈4 in.) diameter.

The objective and eyepiece lenses (L4) form an image of the object plane (i.e., the phase variations on the laser beam) onto the image plane. The lenses are separated from each other by the sum of their focal lengths. A spatial filter (phase mirror) PM1 is placed at the focal point of the lenses. This arrangement produces a demagnified and collimated beam containing an image of the phase variations, at the object plane, onto the detectors (D1) at the image plane. The demagnification factor is ≈4.82, resulting in a beam diameter of ≈1.93 cm. The objective and eyepiece lenses Fourier transform the projection twice, so that an inverted image of the variations at the object plane is produced.

The effect of the apertures on the imaging quality of the system can be thought of as a convolution of the spatial or k spectrum of the object with an Airy function that represents the spectrum of the limiting (circular) aperture. As this Airy function is very well localized (i.e., the distance to the second zero is less than 1 mm), the effect of the apertures on the k spectrum of the light at the focal plane is expected to be insignificant.

In addition to the imaging optics, there is a water-cooled shutter S1 that can block the beam, a Brewster stack BS1 used as a beam attenuator, an ultrasonic speaker SP1 used for calibration purposes, and a bolometer D2 used for monitoring the total laser beam power. A 1.5 mW HeNe laser (HN1), irises I1 and I2, and mirrors M12 and M13 are all used to align the system.

B. The spatial filter

The phase mirror is placed at the focal plane of the objective lens, where it operates on the Fourier transform of the light distribution from the object plane. It consists of a 5-cm (≈2 in.)-diam optic made of ZnSe, with one half coated with gold and raised by 0.41 μm, for a phase shift of ≈28°. Figure 2 provides a schematic diagram of the mirror.

The distance of the vertical step in the mirror from the focal spot determines a high-pass wave number cutoff (k_{cut}). Moving the phase mirror in the horizontal direction thus amounts to a scan of cut-off wave numbers, with mapping $k_{\mathrm{cut}}=11.18\ x_f$ between the wave number (cm^{-1}) and the phase mirror displacement (cm). The resultant transfer function is a step function with a 28° phase shift between positive and negative sidebands. Numerical simulations demonstrate that spatial filtering with this phase mirror will result in adequate recovery of a plasma image.[5]

Phase fluctuations on the laser beam are converted to intensity fluctuations, with a contrast enhancement factor γ, as shown by the following equation:

$$\frac{\Delta I}{I}=\gamma\Delta\phi, \tag{1}$$

where ΔI is the intensity fluctuation that results from a phase fluctuation $\Delta\phi$, and I is the dc component of ΔI. γ is equal to $1/\sqrt{2}\,(1-\sqrt{(2b^2/a^2)-1})$, where a^2 and b^2 are the reflectivities of each half of the phase mirror, also marked in Fig. 2. a^2 and b^2 can be specified (by a choice of materials and coatings) to increase the contrast enhancement factor without altering the imaging properties of the filter. This may be necessary in the case of a weak density fluctuation signal or a high noise floor. γ is evidently maximized for $b^2=1$ (i.e., a purely reflective surface such as gold), and varies with a^2 as shown in Fig. 3. It can be seen that the contrast enhancement can be boosted significantly by reducing a^2. Reduction of a^2 significantly below 5% may be undesirable, however, as then the zeroth order of the laser beam is attenuated to levels comparable to its sidebands. The system responsivity, which

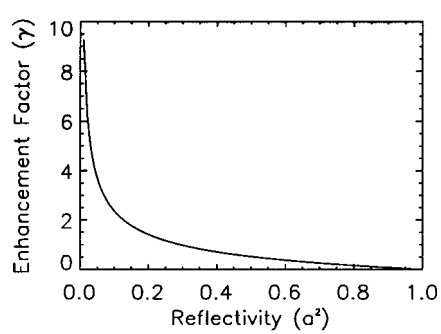

FIG. 3. Enhancement factor (γ) vs reflectivity (a^2).

scales with the total beam power, will likely become more vibration sensitive and inconsistent across the beam cross section.

For the present experiment, bare gold and antireflection (AR) coated ZnSe, yielding $b^2=1$, $a^2=0.17$, and $\gamma\approx1.6$ were used. This phase mirror was most simple and inexpensive to build, and calculations indicated that the resulting system sensitivity would be sufficient.

C. The laser

A CO_2 laser operating at 10.6 μm provides a collimated and coherent light source for imaging. Good transverse electromagnetic $(TEM)_{00}$ mode purity is obtainable, with a $1/e$ radius of $\approx$0.28 cm at the laser output coupler. A nearly confocal arrangement with an aperture placed on the mirror is used to minimize interaction of the beam with the edge of the laser bore. The linear polarization and (P2) longitudinal mode structure are measured as constant as long as the mode quality is maintained. The laser output power is typically set (by adjusting the gas pressure) to 7 Torr, which results in approximately 8 W of laser power at the output coupler, and 1.5 W of beam power at the detectors. Note that 83% of the beam power is split off onto a bolometer at the phase mirror. The bolometer reading serves as a useful monitor of the laser power level and mode quality. The laser is quite sensitive to thermal variations in the operating room, and needs significant readjustment approximately every 5 h of running time.

D. The detection system

A 16-element, horizontal array of mercury–cadmium–telluride (MCT) photoconductors is used to detect the intensity fluctuations on the laser beam. MCT photoconductors were chosen for their high volts per watt response; they have a bandwidth of 1 MHz. The elements are 0.5 mm square, and spaced 1 mm apart, center to center, for a spatial resolution of $\approx$0.5 cm at the object plane (accounting for the demagnification of the system). The array is mounted in a Dewar and cooled with liquid nitrogen to eliminate thermal noise.

Low noise, transimpedance preamps designed specifically for infrared photoconductors (model KA-S5 manufactured by Kolmar Technologies, Inc.) are used for the first stage of amplification from the detectors. The preamp gain is approximately equal to $4000/V$, where V is the voltage drop across a detector element. The gain has a typical value of about 200.

Great care was necessary to avoid electrical pickup and cross-talk problems. Shielded wire was used for all connections between the detector elements, preamplifiers, and batteries, and ground loops were eliminated where possible. The noise floor of this system is determined by the preamplifiers. It is measured to be $\approx2.64\times10^{-7}$ V/$\sqrt{\text{Hz}}$ (including the preamp gain).

E. Performance of the detection system

Operation of the detection system (i.e., detector elements plus preamps) at its maximum responsivity is crucial for obtaining the highest sensitivity possible to density fluctuations.

The small signal ac voltage response of the detection system, ΔV, to an intensity fluctuation, ΔI, is $\Delta V=G(dV/dI)\cdot\Delta I$, where V and I are the corresponding dc quantities and G is the preamp gain. Maximum responsivity (to fluctuations) thus corresponds to a maximum in the quantity $(dV/dI)(I/V)$, since ΔI scales with I and G scales with $1/V$.

The V versus I curve for a sample detector element is shown in Fig. 4(a). Saturation of the element (i.e., dV/dI approaches zero) with increasing incident intensity is evidenced. The responsivity function, $G(dV/dI)I\propto(dV/dI)I/V$ is plotted in Fig. 4(b) for the same element using the same x axis, but with the values of the total laser beam power (TEM_{00} mode) shown. The responsivity drops rapidly as the beam power is decreased below 0.5 W, but remains fairly constant at its maximum value for powers above 0.5 W to at least 4 W. This flat and maximal response is fortituous since it means that the laser power is permitted to drift over a very large range during an experiment without affecting the (optimal) responsivity of the imaging system. An additional benefit is that the laser can be operated at relatively low power levels that improves the safety of the experiment for the user.

As a reference, the responsivity function lies between 8 and 12 V in the optimal operating regime. D_S^* is $\approx2\times10^{13}$ cm$\sqrt{\text{Hz}}$/W, and the detector element responsivity is $\approx$200 V/W.[8]

F. Data acquisition

The signal from the detection system is connected via coaxial cable to a second stage preamplifier (EG&G model M113) that has a gain ranging from 10 to 10 000 and a double pole high-pass filter. The total gain over both stages,

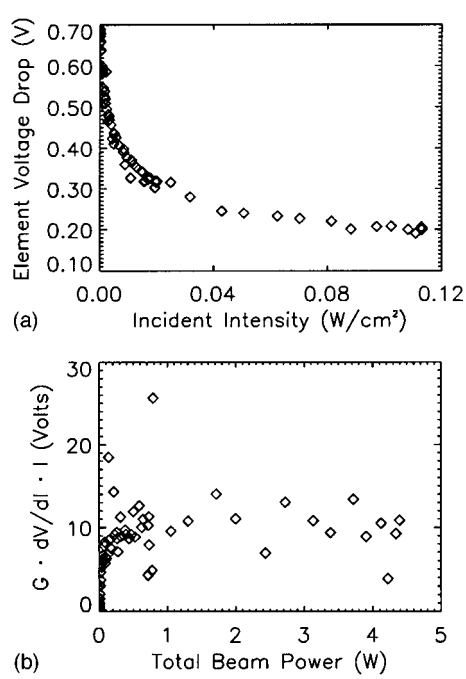

FIG. 4. (a) V vs I curve for a sample detector element. (b) Plot of the detector-preamp responsivity function vs total beam power.

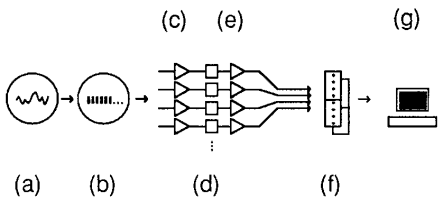

FIG. 5. Schematic diagram of the data acquisition system: (a) laser beam with fluctuation profile; (b) 16-element photoconductor array; (c) 46 dB first amplifier stage; (d) 6 dB/octave high-pass filter stage; (e) second 20–80 dB amplifier stage; (f) 4 LeCroy 6810 digitizers; (g) Quadra 800 Macintosh computer with LABVIEW software.

applied to the detector signal, is typically 10 000. High-pass filtering is essential to remove the low frequency fluctuations in the laser output power caused by electrical pickup. The conditioned signal is then digitized by four 6810 modules that are installed in a CAMAC crate and interfaced to a Quadra 800 Macintosh computer through GPIB. The 6810 modules have the capability to sample 16 channels at 1 MHz. LAB VIEW software is used to control the digitizers from the Quadra, and also to provide real time spectral analysis of the imaging data. The elements of the data acquisition system for the experiment are shown schematically in Fig. 5.

III. CALCULATING THE SYSTEM RESPONSIVITY

The responsivity of the system ($\mathscr{R}$) is its V/cm^{-3} gain and it relates the amplitude of the voltage produced by the detection system (ΔV) to the amplitude of the density fluctuation at the object plane (Δn). Hence

$$\Delta V = \mathscr{R} \Delta n. \tag{2}$$

$\mathscr{R}$ can be readily calculated if each instrumental component of the system is well characterized. This procedure is more reliable than the standard method of imaging sound waves of known amplitude that is also discussed. Once $\mathscr{R}$ is known, the absolute sensitivity of the imaging system can be determined.

The tangential imaging system responsivity is governed by three factors that are common to all PCI systems. The first is the relationship between density fluctuations and the line integrated phase shift impressed on the outgoing laser beam. It has been shown[5] for a tangential beam that the phase variations are equal to the density fluctuations localized to the tangency plane, multiplied by a transfer function H in wave number (k) space:

$$\Delta \phi(k_x) = \eta H(k_x) \Delta n(k_x), \tag{3}$$

where $\eta \approx 2.97 \times 10^{-20}$, and $H(k_x) = \sqrt{(R_0/k_x)} \times e^{\mathrm{sgn}(k_x) i \pi/4}$. R_0 is the major radius of CDX-U ($\approx$0.37 m).

It should be noted that this transfer function brings about a wave number dependence in the system responsivity that does not occur in standard, nontangential PCI systems. This enhanced sensitivity to high wave numbers (i.e., long wavelengths), however, is an integral part of the localization scheme for this diagnostic.

Second, the phase variations are converted to intensity variations at the phase mirror where a contrast enhancement factor is applied, as described in Sec. II B:

$$\frac{\Delta I}{I_0} = \gamma \Delta \phi. \tag{4}$$

Finally, the beam forms an image on the detector plane where the intensity variations are converted to a voltage signal. The voltage is determined by the detection system responsivity as described in Sec. II E:

$$\Delta V = G \left(\frac{dV}{dI} I \right) \frac{\Delta I}{I}. \tag{5}$$

The overall system responsivity to density fluctuations at the tangency plane can thus be written as

$$\mathscr{R} = G \left(\frac{dV}{dI} I_0 \right) \gamma \eta \sqrt{\frac{R_0}{k_x}}, \tag{6}$$

where the phase factor in H has been removed by the phase mirror.

Equation (6) shows how the system responsivity function depends on three independent instrumental factors. The latter two involve the phase mirror and the detection system, and their values have been determined. Hence $\mathscr{R}$ is known and one can predict the system response to a given density or phase fluctuation:

$$\Delta V \approx 2.92 \times 10^{-19} \frac{\Delta n(k_x)}{\sqrt{|k_x|}} \approx 16.13 \Delta \phi. \tag{7}$$

This calculation is expected to be quite accurate as long as the optical component of the system behaves ideally, that is, extraneous diffraction effects are minimized by a careful beam/optic alignment, and all of the optical surfaces have sufficient flatness so as not to disturb the phase front of the beam.

A. Use of sound waves to determine $\mathscr{R}$

The responsivity of the system can also be measured using sound waves. A sound wave radiation pattern is generated by a high frequency speaker placed to emit the waves into the object plane of the system. Figure 1 shows the speaker, SP1 that was moved aside while the CDX-U plasma is being imaged. For calibration purposes, however, the optical table is pulled away from the tokamak and the speaker is mounted along the object plane marked ''O.''

The laser beam passes through the radiation pattern of the speaker and is phase shifted by pressure variations produced by the sound waves. The equation for the phase shift is given by

$$\Delta \phi = k_0 \int_{-z_0}^{+z_0} \Delta n_i \, dl, \tag{8}$$

$$= \frac{2 \pi k_{\mathrm{GD}}}{\lambda_0 R T} \int_{-z_0}^{+z_0} \Delta P \, dl, \tag{9}$$

where $n_i - 1 = k_{\mathrm{GD}} P R T$ has been used. k_{GD} is the empirically determined Gladstone–Dale constant for air, ΔP is the pressure fluctuation of the sound wave, n_i is the index of refraction of air, and P, R, and T are the background air pressure, ideal gas constant, and background air temperature, respectively.[9] The z coordinate runs along the line-of-sight

of the beam. $\int_{-z_0}^{+z_0}\Delta P dl$ is measured by scanning a calibrated microphone across the face of the speaker and along the sightline where the laser measurement will be taken. A $\frac{1}{4}$ in. free field microphone (model 7016), purchased from ACO Pacific, Inc., was used for this purpose.

The system response (ΔV) to the sound waves permits calculation of the instrumental factor $(G(dV/dI)I)\gamma$, and hence system responsivity $\mathscr{R}$ [see Eqs. (6) and (7)]. This procedure, however, was found to be unreliable: the difficulty in aligning the laser with the axis of the microphone scan and the frequency responses of the speaker and microphone produce large uncertainties in the resulting values for $\mathscr{R}$. Lack of an isotropic speaker and lack of adequate room in the experimental area prevented a laser measurement of the sound wave far field that, for a spherical wave, can be calculated with a simple equation. The simple equation that has been used by other PCI experimentalists,[2–4] would likely yield a more accurate result. However, for the present system, the calculation of $\mathscr{R}$ from instrumental factors is felt to be adequate.

Sound wave measurements are useful for other purposes where knowledge of the absolute sound wave radiation pattern along a laser sightline is not needed (as will be discussed).

B. Calculation of the absolute system sensitivity

The absolute system sensitivity is the density fluctuation amplitude at which the signal-to-noise ratio (SNR) is equal to 1 over the measurable bandwidth. It can be thought of as the smallest amplitude density fluctuation that can be imaged by the diagnostic. As is typical of PCI systems, the sensitivity depends on two competing factors, the system responsivity and the noise floor.

The detection system output limits the system noise floor to a value of $\Delta V_{\text{noise}} \approx 2.64\times10^{-7}(\text{V}/\sqrt{\text{Hz}})$. Setting the condition $\Delta V(k_x)=\Delta V_{\text{noise}}$ for a SNR of 1 in Eq. (7) yields an absolute sensitivity of $\Delta n(k_x)_{\min} \approx 9.04\times 10^{11}\sqrt{|k_x|}$, in mks units. Converting to more commonly used cgs units yields

$$\Delta n(k_x)_{\min} \approx 9.04\times10^{6}\sqrt{|k_x|}\,\frac{\text{cm}^{-3}}{\sqrt{\text{Hz}}}\,. \tag{10}$$

$\Delta n(k_x)_{\min}$ is plotted as a function of wave number in Fig. 6. Its variation occurs within an order of magnitude, with a median value of $\approx 1\times10^{7}(\text{cm}^{-3}/\sqrt{\text{Hz}})$. If the transfer function is not included in the calculation, and a 1 m integration length is used instead, one finds a system sensitivity that compares well with other PCI experiments: $\Delta n_{\min} \approx 6\times10^{8}\ \text{cm}^{-3}$ over a 1 MHz bandwidth (cf. Appendix A for a discussion on integration lengths). The corresponding phase sensitivity is independent of wave number and is given by

$$\Delta\phi_{\min} \approx 2\times10^{-8}\,\frac{\text{rad}}{\sqrt{\text{Hz}}}\,. \tag{11}$$

The calculations show that the imaging system should be capable of resolving the density fluctuations on CDX-U,

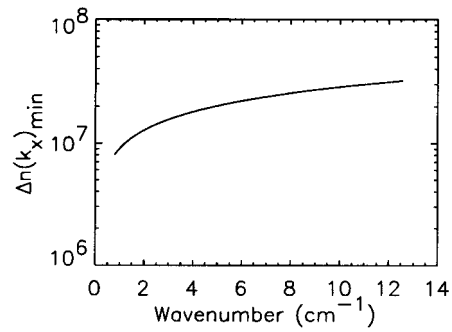

FIG. 6. Absolute sensitivity of the diagnostic, $\Delta n(k_x)_{\min}$, vs wave number.

where the background densities (n_0) are typically $2\text{–}3\times10^{12}$ cm^{-3}, and $\Delta n/n_0 \approx 1\%$ over a bandwidth of 40 kHz.

IV. IMAGE PLANE LOCATION

The image plane is uniquely specified once the object plane is fixed at either the plasma tangency plane or speaker location. Inaccurate placement of the detector array at the image plane can result in a poor cutoff and also in distortion of the k spectrum of the object.

A. Methods I and II

Fresnel diffraction theory yields the following equation that relates the location of the image plane to that of the object plane:

$$\left(\frac{1}{f_{\text{obj}}}-\frac{1}{d_{\text{obj}}}-\frac{1}{d_{\text{img}}}\right)\left(\frac{1}{f_{\text{eye}}}-\frac{1}{d_{\text{img}}}-\frac{1}{d_{\text{int}}}\right)=\frac{1}{(d_{\text{img}})^2}. \tag{12}$$

f_{obj} and f_{eye} are the focal lengths of the objective and eyepiece lenses (L3 and L4), respectively, d_{obj} is the distance between L3 and the object plane, d_{int} is the interoptic distance between the lenses, and d_{img} is the distance between L4 and the image plane. f_{obj}, f_{eye}, and d_{int} are fixed at 5.3, 1.1, and 6.4 m, respectively. All of these optics and optical distances can be viewed in Fig. 1.

Figure 7 shows a plot of Eq. (12). Due to the demagnification factor, a $\approx$1 m variation of the object plane results in only a $\approx$5 cm variation of the image plane. This is a desirable feature, as fine-tuning adjustments of the detector array position are thus sufficient to scan through a wide range of possible object plane locations.

Calculation of d_{img} from d_{obj} with Eq. (12) is only approximate however, as slight errors in the values for the in-

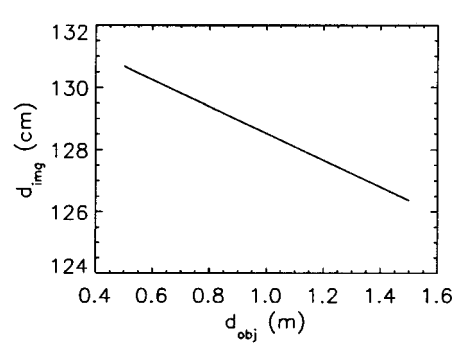

FIG. 7. Plot of d_{img} (image plane location) vs d_{obj} (object plane location).

teroptic distances and optical alignment have a large, cumulative effect on the results. A superior method was to mount a metal template with many fine-scale perforations at the object plane (and in the path of the laser beam). A fluorescent viewing screen was used to find the image plane, i.e., where the image of the template was most sharply in focus. The accuracy of the method is still limited to $\approx\pm 20$ cm (in the object plane) compared to the measurement that will be described next.

B. Method III: Beam diffraction measurement

1. Diffraction from a phase object

In the absence of phase contrast, the image of a phase object is a phase variation so the signal level measured at the image plane should be close to zero. The measured signal level, however, will increase with distance as one moves away from the image plane. This is a consequence of the diffraction of the laser beam as it propagates. More specifically, as shown in Appendix B, a sinusoidal phase disturbance, given by $\phi_0 \sin(k_x x+\theta)$ at the object plane, results in a diffraction signal that increases linearly with distance from the image plane:

$$\Delta I_{\mathrm{diff}} \approx \left(-\frac{1}{2}\frac{k_x^2}{k_0}\right)\cdot \Delta z_{\mathrm{img}} \phi_0 \sin(k_x x+\theta). \tag{13}$$

$\Delta I_{\mathrm{diffr}}$ represents the intensity fluctuation due to diffraction, k_0 is the wave number of the laser beam and z_{img} is the distance along the beam from the image plane. Note that the rate of increase in signal scales with the square of the wave number of the scattering object. Measurement of this linear variation will yield the location of the image plane as the minimum point in the signal level.

2. Measuring the diffraction signal

Replacement of the phase mirror with a gold flat readily eliminates the phase contrast imaging capability of the system. The speaker is placed at the object plane ''O'' and scanned along the z direction. It was easier to scan the object instead of the detectors; since d_{img} and d_{obj} scale almost linearly (see Fig. 7), the result is the same. As the speaker output is tightly collimated in the z direction, it approximates a phase object that is localized to the object plane. A 10 kHz signal is used to excite the speaker, which generates additional harmonics at 20, 30, and 40 kHz.

The results are shown in Fig. 8. A minimum can be roughly located (and is labeled the image plane), with an approximate linear increase in signal away from that point, for all three wave numbers. In addition, the slopes of the lines increase with wave number at roughly the expected rate. Scatter in the data points is produced by multiple reflection of sound waves from surfaces in the lab, and it is due to the fact that the sound waves are not perfectly localized to the object plane.

3. Locating the image plane

During plasma runs when the speaker and tangency plane are displaced by ≈ 0.5 m, the image plane for the speaker is first located by moving the detector array with a vernier. Equation (12) is then used to calculate the additional displacement necessary to locate the image plane of the tangency plane (≈ 2 cm). This method of locating the image plane is quite accurate and minimizes the k-spectrum distortion in the imaging process; it also results in a sharper, more complete cutoff by the phase mirror. The system response is also improved. Unfortunately, a complete beam alignment, followed by an image plane location, results in preparation times of two hours or more before each run. Use of a more stable commercial CO_2 laser would reduce the necessary preparation time.

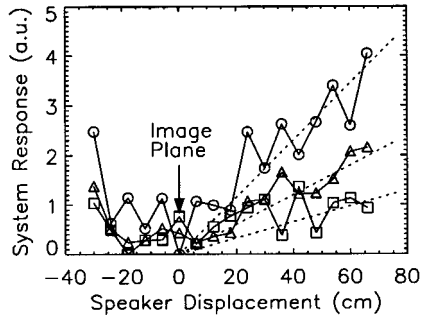

FIG. 8. Results of the diffraction signal measurement. The dashed lines represent linear approximations to the three data sets; circles represent the 40 kHz data; triangles represent the 30 kHz data; and squares represent the 20 kHz data.

The successful measurement of such a small effect as beam diffraction also verifies that significant extraneous diffraction of the beam (by air currents or apertures, for example) is not occurring. Instead, one is confident that the behavior of the optical system is very close to an ideal one that can be modeled by the Fresnel equations for light.

V. TESTS OF IMAGING USING SOUND WAVES

Characteristics of the imaging system, like demagnification, the two imaging regimes of the phase mirror, and its step-function wave number transfer function, can be measured by imaging sound waves. These sound wave measurements are essential to verify that the imaging of phase objects at the object plane onto the image plane is indeed taking place.

A. Measurement of system demagnification

The successful measurement of system demagnification attests to the imaging beam being properly collimated. It is also an indication of how accurately the (spatial) phase is measured by the system. As mentioned previously, one expects phase objects of all wave numbers placed at the object plane to be reduced in size by a factor of 4.82 in the image.

To measure demagnification, sound waves are imaged onto the detector plane. The demagnified wavelength on this plane is determined by measuring the phase difference in the signals from detector elements of known spatial separation. A comparison with the calculated wavelength of the sound wave in air yields the demagnification factor.

Figure 9 shows the measured demagnification as a function of sound wave wave number. The average demagnifi-

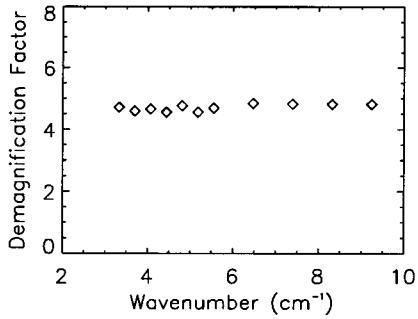

FIG. 9. Measured demagnification factor as a function of sound wave wave number.

cation is 4.71, which is acceptably close to the expected value.

B. Measurement of the imaging regimes

The solid curves in Figs. 10(a) and 10(b) show the variation in the system response for two sample sound wave wave numbers (5.54 and 4.06 cm^{-1}) as the phase mirror is scanned horizontally across the focal plane. The two imaging regimes, represented by regions where the system response is finite and flat, can be clearly seen.

The transition of the focal spot from one side of the phase mirror to the other is monitored by the amount of power passing through the phase mirror and striking the bolometer. This quantity is also plotted as a dotted line. Seventy-one percent of the total beam power is transmitted when the focal spot is on the ZnSe side, whereas the beam is completely reflected by the gold side (0% transmission).

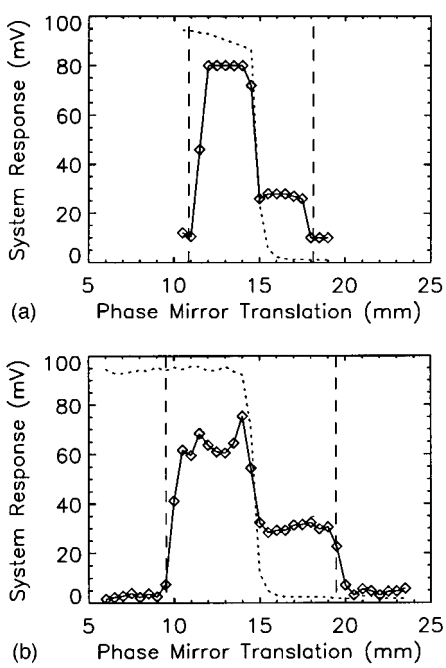

FIG. 10. Variation in the system response as the phase mirror is scanned for two sound wave wave numbers: (a) 5.54 and (b) 4.06 cm^{-1}. Diamonds joined by lines represent the experimental data; short dashes represent the beam power on the bolometer and show the transition of the focal spot from one side of the phase mirror to the other. The long dashes mark the expected cut-off locations.

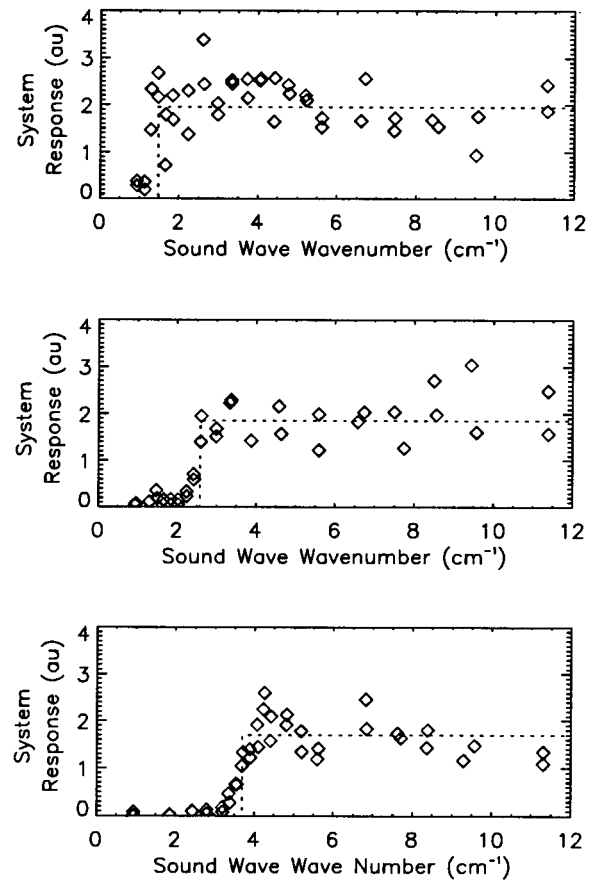

FIG. 11. Plot of the system transfer function as a function of sound wave wave number. Three phase mirror settings are shown corresponding to wave number cutoffs of (a) 1.33, (b) 2.44, and (c) 3.92 cm^{-1}, respectively. The expected high-pass step function nature of the system is clearly in evidence, and the measurements are in rough agreement with the expected cut-off locations. Symbols represent data points, while dashed lines show the expected step function.

Note that the diameter of the focal spot is approximately 1 mm, which is close to that expected from the Airy pattern produced by the limiting aperture.

Quantitative features of the phase mirror scan agree with those predicted by theory. Cutoff of the signal occurs at the expected displacements, marked by dashed lines, for both sample cases. The ratio of the enhancement factors between the two imaging regimes is calculated to be ≈ 2.68, which approximately matches the observed ratio of system response levels.

C. Measurement of the system transfer function

Figures 11(a)–11(c) show plots of the system response as a function of (sound wave) wave number. The expected high-pass, step function transfer function (cf. Sec. II B) is clearly in evidence. The symbols represent data points, while the dashed lines show the expected step function for reference. Figures 11(a)–11(c) correspond to three horizontal phase mirror positions with wave number cutoffs of approximately 1.33, 2.44, and 3.92 cm^{-1}. The measured cutoffs are in rough agreement with those expected from the phase mirror settings. The step function transfer function of the imag-

ing system is thus verified. Note also the flexibility of the phase mirror design to select any particular k_{cut}.

We should also note that the scatter in the sound wave response data is reduced by an order of magnitude if method III (cf. Sec. IV B) is used to locate the image plane. The cutoffs also become sharper and more complete. (Time constraints precluded use of the method for most of the calibration work.) The present data are quite sufficient for demonstrating all of the important characteristics of imaging, however.

VI. IMAGING PLASMA DENSITY FLUCTUATIONS ON CDX-U

A. Introduction and scope

The first objective of the plasma measurements was to verify that the system was capable of imaging plasma density fluctuations on CDX-U. It had to be shown that the system responsivity was adequate and that the added noise produced by the CDX-U tokamak (i.e., rf power sources, magnetic field coils, etc.) did not overwhelm the plasma signals. In addition, assurance was needed that the fluctuation signals were indeed a result of phase contrast imaging of density fluctuations at the object plane, and not a diffraction effect.

The second objective was to observe the effect of scanning k_{cut}, with the phase mirror, on the plasma fluctuations. This would verify that spatial filtering of the plasma k spectrum was possible and that the density fluctuations were in the expected wave number range that is accessible by the diagnostic. Measurement of the fluctuation k spectrum was also desired.

B. Experimental setup

In preparation for plasma measurements, the optical table is pushed onto the CDX-U tokamak as shown in Fig. 1. The speaker is mounted to one side on one of the table arms in order to act as a monitor of system response and performance. By monitoring the amplitude of a 30 kHz sound wave signal throughout all the plasma shots, one can ensure that the system response did not decrease from its expected value for any reason. Cutoff of the sound wave at the expected phase mirror setting also ensures that the focal spot has not wandered on the mirror.

The image plane for the sound waves is located using method III as discussed earlier.

C. Description of a typical CDX-U plasma shot

Figures 12(a)–12(d) show four diagnostic traces of the typical CDX-U plasma shot that was used to test the system. The plasma current is shown in Fig. 12(a). The time period of the plot, from 10.5 to 16 ms, covers the flattest area of the current peak. In this region, the density and temperature are near their highest values. The time period from 12 to 14 ms, when an internal reconnection event (IRE) occurs (indicated by the small spike in the current trace), is analyzed for fluctuations. The plasma in this region is relatively stable and is reproducible from shot to shot. The lower three traces [(b), (c), and (d)] record the line integrated density near the plasma edge (using a microwave interferometer[10]), soft x-ray emissions (from C V in the plasma core[11]), and the system response of the phase contrast imaging system. It can be seen that the fluctuation level begins to rise at 12 ms as the bulk density and temperature also increase. The fluctuations become quite large and unpredictable beyond 14 ms and after the IRE when the plasma is likely moving about and striking the limiters. The density in the time window of interest is measured to be $\approx 8.8\times 10^{11}$ cm^{-3} at the edge (which translates to $\approx 2.2\times 10^{12}$ cm^{-3} in the core), and the temperature is likely to be ≈ 150 eV in the core. In Fig. 12(d), the phase mirror was set to image as much of the k spectrum as possible.

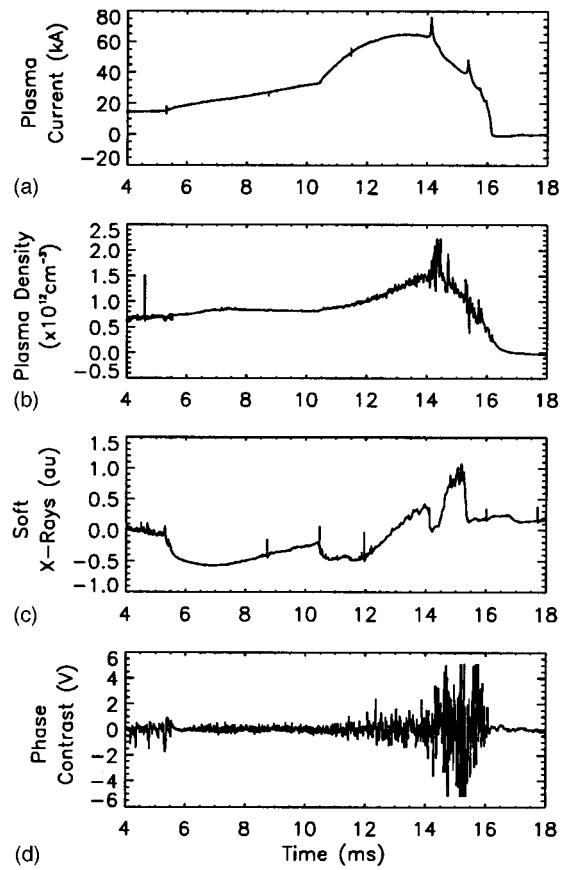

FIG. 12. Four diagnostic traces of the typical CDX-U plasma shot that was used to test the system: (a) plasma current; (b) line integrated density (n_e) near the plasma edge; (c) soft x-ray emission from C V in the core; and (d) the system response from a channel of the phase contrast imaging system.

D. Verification of plasma fluctuations being measurable

Figure 13 shows density fluctuation power spectra for the time window from 12 to 14 ms, as measured by the imaging system. The amplitude of the plasma signal (uppermost trace) is compared with three sources of noise (lower traces): detector-preamp noise, the electromagnetic noise induced on the system when the tokamak is pulsed with no gas, and finally the laser noise. The plasma signal is observed to be at least two to three orders of magnitude greater than all of the background noise sources over the frequency range from 0 to 100 kHz. Calculations indicate a density

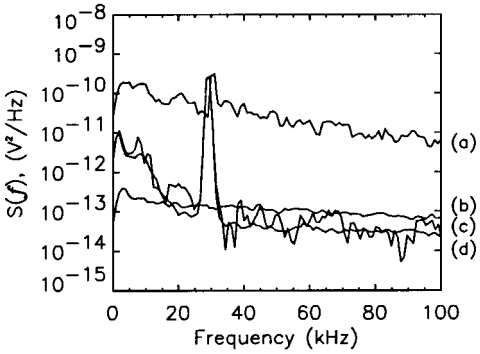

FIG. 13. Four power spectra that compare the density fluctuation signal to three sources of noise: (a) plasma signal; (b) detector-preamp noise; (c) electromagnetic noise from the tokamak; and (d) laser noise.

fluctuation amplitude of $\approx 1.3\times 10^{10}$ cm^{-3}. It is thus verified that the responsivity of the system is adequate, and that the plasma signals are not dominated by extraneous noise. Note that the peak that occurs at 30 kHz is produced by the sound wave monitor.

E. Observation of sawteeth in the plasma core

Evidence that imaging of plasma density fluctuations is taking place is shown in Fig. 14. Data traces from a different type of shot, where significant sawteething behavior was observed, are plotted. The top trace (dashed line) represents the soft x-ray signal, while the lower three traces (solid lines) represent the filtered signal from three adjacent detector elements on the phase contrast imaging detector array. The 5 kHz sawteeth are quite visible on the phase contrast signals; they match the phase and the shape of the peaks on the x rays, leaving little doubt that they are the same fluctuations. These sawteeth are thought to occur in the core plasma only, and not in the edge.

F. Measuring the fluctuation *k* spectrum

A series of plasma shots was taken as the phase mirror was scanned through a sequence of wave numbers. This was done to measure the fluctuation k spectrum and to see if the spectrum could be cut off. The initial results, ensemble averaged for each phase mirror setting, are shown in Fig. 15. One can see a dramatic drop in signal power level over the entire frequency bandwidth as progressively more and more

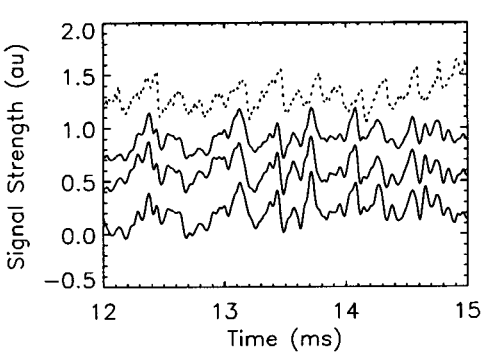

FIG. 14. Plasma sawteeth observed on core soft x rays (top, dashed line), and three phase contrast channels.

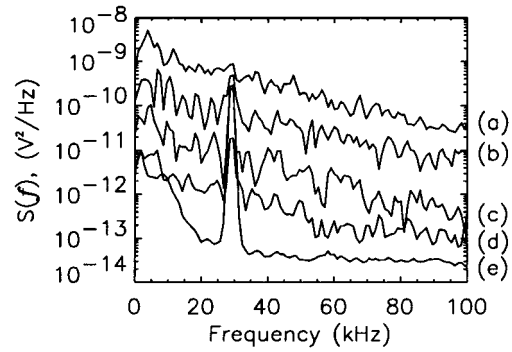

FIG. 15. Power spectra of plasma measurements showing a drop in signal power level as the k spectrum is cut off. The phase mirror is set at the following cut-off wave numbers: (a) 0.59; (b) 1.48; (c) 2.36; and (d) 7.1 cm^{-1}; (e) 1.18 (no plasma case).

of the k spectrum is cut off from the low wave number (long wavelength) side. This suggests that the k spectrum can be measured by this diagnostic.

Note the peak at 30 kHz that represents the sound wave monitor. It gradually becomes visible as the plasma signal drops with phase mirror position. Finally the sound wave itself, which has a wave number of ≈ 5.6 cm^{-1}, is cut off. The sound wave signal indicates that the system response level remains constant throughout the run and that the imaging system is functioning properly.

Figure 16(a) is a plot of the same data as a function of the cut-off wave number (k_{cut}). The signal power over a specific frequency range only (in this case 1–10 kHz) is plotted. One can see the marked drop in signal power (over more than two orders of magnitude) as the cut-off wave number is increased. Scatter in the points is caused by statistical variability between plasma shots that is the main source of experimental uncertainty. The average signal power at each cut-off wave number is plotted as a filled symbol so that the overall trend in the data can be observed more clearly.

The complete cutoff of plasma fluctuation signal by the phase mirror can be seen: beyond $k\approx 4.5$ cm^{-1}, the signal levels are at diffraction effect levels. This is an important verification that the measured signal is produced by phase contrast imaging of plasma fluctuations at the object plane and that significant diffraction of the beam by plasma inhomogeneities is not taking place (see also Sec. IV B 3).

Note that Fig. 16(a) represents $\int_{k_{\mathrm{cut}}}^{\infty}(1/k)\tilde{S}(k)dk$ (stationarity and spatial uniformity of the fluctuations are assumed), where $\tilde{S}(k)$ is the fluctuation spectrum as a function of wave number. $\tilde{S}(k)$ itself can be determined by taking the derivative of the function with respect to k_{cut} and then multiplying by k.

The derivative function is shown in Fig. 16(b). This curve represents $(1/k)\tilde{S}(k)$, although one can see that its rolloff with k is too steep to be attributed to the $1/k$ effect [caused by the plasma transfer function $H(k)$] alone. Removal of the $(1/k)$ factor results in the function plotted in Fig. 16(c), which should represent $\tilde{S}(k)$. One can see how the power in the fluctuating k spectrum is concentrated between 1 and 3 cm^{-1}.

Figure 16(d) shows the spectral power in the soft x-ray

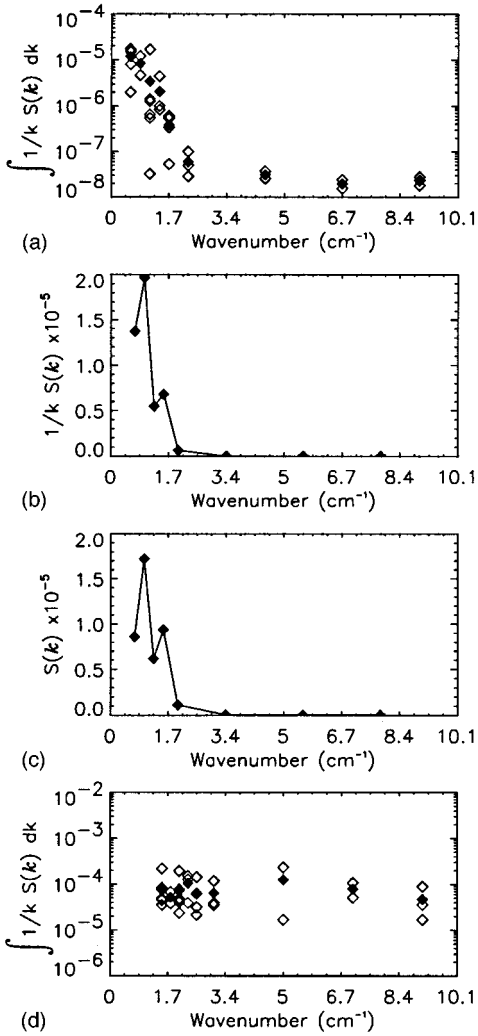

FIG. 16. Density fluctuation data from 1 to 10 kHz as a function of cut-off wave number (k_{cut}): (a) power in the system response from a phase contrast channel; (b) the derivative of curve (a); (c) the calculated k spectrum; and (d) the power in the soft x-ray emissions which show that the plasma fluctuation level remains constant. Unfilled diamonds represent individual shots; the filled diamonds represent average values for a given phase mirror setting.

fluctuation signal over the same frequency band that was taken simultaneously with the phase mirror scan. The signal level holds relatively constant, which provides some assurance that the plasma fluctuation level in CDX-U is not changing over the duration of the run. Although results from only one frequency band are shown here, the curves are quite similar over the entire frequency range from 0 to 100 kHz.

G. Summary of the plasma measurements

Two important components of the proof-of-principle for the tangential phase contrast imaging system were demonstrated by the plasma measurements described above. First, it was verified that measurable plasma signals could be obtained. The system responsivity and noise levels were acceptable, direct correlation with core measurements made by soft x-ray spectroscopy was observed in the sawteeth fluctuations, and a cutoff of the fluctuations was observed, verifying that phase contrast imaging of the object plane was taking place. Second, a phase mirror scan produced a significant variation in the fluctuation signal levels. The effect of the phase mirror as a spatial filter on the fluctuation of the k spectrum was demonstrated. More important, we found that the plasma fluctuations have a k spectrum that ranges from ≈ 1 to 3 cm^{-1}, which is in the expected range of interest for the imaging diagnostic.

VII. CONCLUSIONS AND FUTURE WORK

The novel CO_2 laser-based tangential phase contrast imaging diagnostic was characterized and calibrated. The diagnostic is found to operate successfully as an imaging system. Imaging of plasma fluctuations was successful.

The remaining issue in the proof-of-principle demonstration is verification that localized measurements are possible. Specifically, it must be confirmed that the transfer function discussed in Sec. II B and in Ref. 5 represents an adequate description of the plasma's effect on the laser beam. More detailed correlation with other fluctuation diagnostics on CDX-U will help to clarify this issue.

ACKNOWLEDGMENTS

The authors wish to thank the CDX-U group, and also Josh Breslau for his help with the LabView software. This work was supported by U.S. Department of Energy Contract No. DE-AC02-76CH03073.

APPENDIX A: DISCUSSION OF INTEGRATION LENGTHS

With the tangential imaging geometry and associated inversion scheme, we attempt to eliminate the ambiguity in the phase shift measurement caused by the line of sight integration of density fluctuations. An effective integration length can be calculated for the system, however, that serves as a useful parameter for understanding system sensitivity. The length can be thought of as the thickness of plasma required to produce the same phase shift if the plasma were a slab of uniform thickness transverse to the beam and containing the same sinusoidal density variation.

From earlier equations it can be seen that

$$\int_{-z_0}^{+z_0} \Delta n(k_x)\,dz \approx \sqrt{\frac{R_0}{k_x}}\,\Delta n(k_x); \tag{A1}$$

therefore,

$$l_{\mathrm{eff}} = \sqrt{\frac{R_0}{k_x}}, \tag{A2}$$

where l_{eff} is the effective integration length.

Note that the larger the radius of curvature of the field lines, the longer the effective integration length, and hence the greater the sensitivity of the technique to localized density fluctuations. Typical integration lengths are

$$l_{\mathrm{eff}} \approx 1.72 \ \mathrm{cm} \quad \text{for } k_x = 12.6 \ \mathrm{cm}^{-1}, \tag{A3}$$

$$l_{\mathrm{eff}} \approx 4.85 \ \mathrm{cm} \quad \text{for } k_x = 1.57 \ \mathrm{cm}^{-1}. \tag{A4}$$

The integration lengths are small compared to the size of the plasma, which reflects the fact that a measurement of the

density fluctuation localized to the tangency plane is taking place. In the typical vertical-beam PCI system integration lengths would be equal to the cross-sectional diameter of the plasma, i.e., ≈ 1 m.

APPENDIX B: DIFFRACTION OF THE LASER BEAM NEAR THE IMAGE PLANE

The light distribution at the object plane for a sinusoidal phase disturbance $\phi_0 \sin(k_x x+\theta)$ can be written as

$$u(x,y,0)=e^{j\phi_0 \sin(k_x x+\theta)}, \tag{B1}$$

$$\approx 1+j\phi_0 \sin(k_x x+\theta), \tag{B2}$$

$$=1+\frac{\phi_0}{2}\left(e^{+j(k_x x+\theta)}-e^{-j(k_x x+\theta)}\right), \tag{B3}$$

where $u(x,y,z)$ is the light amplitude function with the object plane located at $z=0$.

The propagation of this distribution is most conveniently described by the angular spectrum model for diffraction:[12]

$$u(x,y,z)=e^{j(kz)}+\frac{\phi_0}{2}\left(e^{+j(k_x x+\gamma z+\theta)}-e^{-j(k_x x-\gamma z+\theta)}\right), \tag{B4}$$

where $\gamma=1/\lambda\sqrt{1-(\lambda k_x)^2}$ is the unscattered wave number component in the direction of propagation.

The intensity distribution for small displacements z from the object plane is thus

$$I=|u|^2, \tag{B5}$$

$$\approx |u_0|^2+u_0^*\phi_0 \sin[(\gamma-k_0)\Delta z]\sin(k_x x+\theta), \tag{B6}$$

$$\approx |u_0|^2-u_0^*\phi_0\left(\frac{1}{2}\frac{k_x^2}{k_0}\right)\Delta z \sin(k_x x+\theta). \tag{B7}$$

$k_0=\sqrt{k_x^2+\gamma^2}$ is the total wave number of the laser light. Hence a linear increase in signal with distance from the image plane is expected, with the slope of the variation scaling with the wave number of the object. This effect is simply a consequence of the propagation and interference of the various k components of the laser light and is termed ''diffraction.'' [11]

[1] Y. S. Hwang *et al.*, Proceedings of the 15th IAEA International Conference on Plasma Physics and Controlled Nuclear Fusion Research, Seville, Spain, 26 September–1 October 1994 (unpublished), Vol. 1, p. 737.
[2] H. Weisen *et al.*, Plasma Phys. Control. Fusion **28**, 1161 (1986).
[3] S. Coda, M. Porkolab, and T. N. Carlstrom, Rev. Sci. Instrum. **63**, 4974 (1992).
[4] K. Tanaka *et al.*, J. Phys. Soc. Jpn. 1 **62**, 3092 (1993).
[5] E. Lo, J. Wright, and R. Nazikian, Rev. Sci. Instrum. **66**, 1180 (1995).
[6] R. Nazikian and B. Grek, Rev. Sci. Instrum. **61**, 2899 (1990).
[7] A. E. Seigmann, *Lasers* (University Science Books, Mill Valley, CA, 1986).
[8] *The Infrared Handbook*, edited by W. L. Wolfe and G. J. Zissis (Office of Naval Research, Department of the Navy, Arlington, VA, 1978), Chap. 11.
[9] G. W. C. Kaye and T. H. Laby, *Tables of Physical and Chemical Constants* (Longman, New York, 1986), Chap. 17.
[10] C. B. Forest, Rev. Sci. Instrum. **61**, 2888 (1990).
[11] D. Stutman *et al.*, Rev. Sci. Instrum. **68**, 1055 (1997).
[12] J. W. Goodman, *Introduction to Fourier Optics* (McGraw-Hill, New York, 1988), pp. 48–53.